

**NICKEL SULFIDE NANOSTRUCTURES
FOR HIGH PERFORMANCE
SUPERCAPATTERY APPLICATIONS**

M.Tech. Thesis

By
DIWAKAR SINGH



**DEPARTMENT OF METALLURGY
ENGINEERING AND MATERIALS SCIENCE
INDIAN INSTITUTE OF TECHNOLOGY
INDORE**

JUNE 2022

**NICKEL SULFIDE NANOSTRUCTURES FOR
HIGH PERFORMANCE SUPERCAPATTERY
APPLICATIONS**

A THESIS

*Submitted in partial fulfillment of the
requirements for the award of the degree*

of
Master of Technology

by
DIWAKAR SINGH



**DEPARTMENT OF METALLURGY ENGINEERING
AND MATERIALS SCIENCE
INDIAN INSTITUTE OF TECHNOLOGY
INDORE**

JUNE 2022



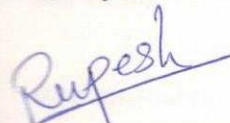
INDIAN INSTITUTE OF TECHNOLOGY INDORE

CANDIDATE'S DECLARATION

I hereby certify that the work which is being presented in the thesis entitled **Nickel sulfide nanostructures for high performance supercapattery applications** in the partial fulfillment of the requirements for the award of the degree of **MASTER OF TECHNOLOGY** and submitted in the **Department of Metallurgy Engineering and Materials Science, Indian Institute of Technology Indore**, is an authentic record of my own work carried out during the time period from August 2020 to June 2022 under the supervision of Dr. Rupesh S. Devan and Dr. Santosh S. Hosmani. The matter presented in this thesis has not been submitted by me for the award of any other degree of this or any other institute.

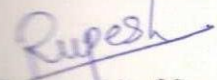

(DIWAKAR SINGH)

This is to certify that the above statement made by the candidate is correct to the best of our knowledge.

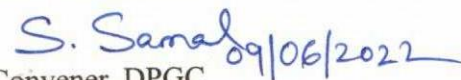

(Dr. RUPESH S. DEVAN)

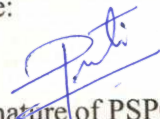

(Dr. SANTOSH S. HOSMANI)

DIWAKAR SINGH has successfully given his M.Tech. Oral Examination held on 3rd June 2022.


Signature(s) of Supervisor(s) of M.Tech. thesis
Date: 03/06/2022


Signature of PSPC Member #1
Date: 03.06.2022


Convener, DPGC
Date: 09/06/2022


Signature of PSPC Member #2
Date: 03/06/2022

ACKNOWLEDGEMENTS

Foremost, I would like to express my sincere gratitude to my Supervisor, Dr. Rupesh S. Devan, for the continuous support of my M.Tech. study and research, for his patience, motivation, enthusiasm, and immense knowledge. His guidance helped me in all the time of research and writing of this thesis. I could not have imagined having a better Supervisor and mentor for my M.Tech. study. I am also thankful to my co-supervisor, Dr. Santosh S. Hosmani, for his timely advice. Besides my supervisors, I would like to thank the rest of my thesis committee members: Dr. Sunil Kumar and Dr. Preeti A. Bhoje, for the encouragement, insightful comments, reviews, and evaluation.

I would also like to thank my lab-mates from Nano-architectures Research Group, IIT Indore, for their continuous support, company, and motivation. Thank Mr. Vishesh Manjunath, Mr. Santosh Bimli, Ms. Sameena Mulani, Ms. Samtham Manopriya, Ms. Ekta Chaudhary, and Mr. D. Yashwanth Reddy for all the group discussion, and company we had during my entire thesis project work.

Last but not the least, I express my endearing gratitude to my family and friends for their unconditional love, support, and patience that enabled me to achieve my goals, and I dedicate this thesis to them.

Abstract

In this study, we engineered Nickel Sulfide (NiS) nanosheets using the Hydrothermal method by optimizing various parameters such as concentration, temperature, and time. X-ray diffraction confirmed the synthesis of crystalline nickel sulfide in two phases- namely millerite and hexagonal. We used Rietveld refinement to quantify the two phases, and it showed that Millerite and Hexagonal phases were present at 96.97 and 3.03 percent, respectively. BET showed the surface area for the synthesized NiS to be 9.7 m²/g. The synthesized Nickel Sulfide was drop cast on Ni foam with the Nafion binder and tested for energy storage in a three-electrode pattern. Cyclic voltammetry showed that the NiS behaves like a battery-type electrode. Galvanostatic charge-discharge studies revealed that the NiS possesses a high specific capacity of 219 mAh/g at 1 A/g and excellent specific capacitance of 2693 F/g at 1 A/g. We also studied the cyclic stability at the current density of 2 A/g, and capacitance retained after 2,500 cycles was 73.6%. Corrosion studies showed that the corrosion rate was higher initially but reduced and became almost constant after 200 cycles. Hence, NiS nanosheets should be promising electrode materials for futuristic supercapatteries.

LIST OF PUBLICATIONS

1. **Diwakar Singh**, et al. "Synthesis and corrosion studies of nickel sulfide nanostructures for high performance supercapattery applications". (Under preparation)
2. Narasimharao Kitchamsetti, Manopriya Samtham¹, Diwakar Singh¹, Sachin R. Rondiya, Yuan-Ron Ma, Russel W. Cross, Parasharam M. Shirage, Nelson Y. Dzade, Rupesh S. Devan* "High performance supercapacitor electrodes of hybrid porous core-shell structure of hierarchical MnO₂ nanoflakes and mesoporous NiTiO₃ nanorods" *Journal of energy storage* (**Under review**) [1: authors share equal contribution] [I.F. = 6.583]
3. Samtham Manopriya, **Diwakar Singh**, K. Hareesh, and Rupesh S. Devan. "Perspectives of conducting polymer nanostructures for high-performance electrochemical capacitors." *Journal of Energy Storage* 51 (2022): 104418. [I.F. = 6.583]
4. Narasimharao Kitchamsetti, Manopriya Samtham, Pravin N. Didwal, Dharendra Kumar, **Diwakar Singh**, Santosh Bimli, Parameshwar R. Chikate et al. "Theory abide experimental investigations on morphology driven enhancement of electrochemical energy storage performance for manganese titanate perovskites electrodes." *Journal of Power Sources* 538 (2022): 231525. [I.F. = 9.127]
5. Mohamed Alla, Vishesh Manjunath, Najwa Chawki, **Diwakar Singh**, Subhash C. Yadav, Mustapha Rouchdi, Fares Boubker. "Optimized CH₃NH₃PbI_{3-x}Cl_x based perovskite solar cell with theoretical efficiency exceeding 30%." *Optical Materials* 124 (2022): 112044. [I.F. = 3.08]

TABLE OF CONTENTS

| | |
|---|-------------|
| List of Figures | vi |
| List of Tables | vii |
| Nomenclature | viii |
| Acronyms | ix |
| | |
| Chapter 1: Introduction | 1 |
| 1.1 Need for energy storage | 2 |
| 1.2 What is a capacitor? | 2 |
| 1.3 What is supercapacitor? | 2 |
| 1.4 Types of Supercapacitor | 3 |
| 1.5 Comparison of batteries and supercapacitors | 4 |
| 1.6 Literature review | 5 |
| 1.7 Research Gaps | 6 |
| 1.8 Objectives | 7 |
| | |
| Chapter 2: Experimental Section | 9 |
| 2.1 Material Synthesis | 10 |
| 2.2 Material Characterization | 10 |
| 2.2.1 Field emission scanning electron microscope | 10 |
| 2.2.2 Energy Dispersive X-ray Spectroscopy | 10 |
| 2.2.3 X-Ray Diffraction | 11 |
| 2.2.4 X-ray Photoelectron Spectroscopy | 11 |
| 2.2.5 BET Surface area analysis | 11 |
| 2.3 Electrochemical Characterization | 12 |
| 2.3.1 Cyclic Voltammetry | 13 |
| 2.3.2 Galvanostatic Charge Discharge | 15 |
| 2.3.3 Electrochemical Impedance Spectroscopy | 15 |
| 2.4 Corrosion studies | 16 |
| 2.4.1 Open Circuit Potential | 16 |
| 2.4.2 Linear Sweep Voltammetry | 16 |
| | |
| Chapter 3: Results and Discussion | 19 |
| 3.1 Material Characterization | 20 |
| 3.1.1 Field emission scanning electron microscopy | 20 |
| 3.1.2 Energy Dispersive X-ray Spectroscopy | 20 |
| 3.1.3 X-ray Photoelectron spectroscopy | 21 |

| | | |
|--|----------------------------------|-----------|
| 3.1.4 | X-Ray Diffraction | 22 |
| 3.1.5 | BET surface area analysis | 23 |
| 3.2 | Electrochemical Characterization | 23 |
| 3.2.1 | Cyclic Voltammetry | 24 |
| 3.2.2 | Galvanostatic Charge Discharge | 25 |
| 3.2.3 | Cyclic stability and EIS | 26 |
| 3.3 | Corrosion studies | 27 |
| Chapter 4: Conclusions and Future Scope | | 31 |
| 4.1 | Conclusions | 32 |
| 4.2 | Future Scope | 32 |
| References | | 33 |

LIST OF FIGURES

- Figure 1.1 Typical construction of a supercapacitor
- Figure 1.2 Specific capacitance of different materials
- Figure 2.1 Cyclic voltammetry (a,b,d,e,g,h) and their corresponding GCD curves for various types of energy storage
- Figure 2.2 Significance of slope of Log (i_p) vs. log (sweep rate) for determining behavior of electrode
- Figure 3.1 FESEM images of NiS nanosheets
- Figure 3.2 EDS spectra of as-synthesized NiS nanosheets
- Figure 3.3 High-resolution XPS Spectra of (a) Ni(2p); (b) S(2p); and (c) O(1s) core levels of the NiS nanosheets
- Figure 3.4 Rietveld refined XRD of NiS nanosheets along with residual curve located at the bottom.
- Figure 3.5 (a) N₂ adsorption-desorption isotherm, and (b) BJH pore size distribution of the NiS nanosheets
- Figure 3.6 (a) Cyclic voltammograms of NiS nanosheets at various scan rates in 1M aq. KOH electrolyte. The graphical illustration of (b) log of peak current density (i_p) vs log of scan rate, and; (c) specific capacitance at various scan rates , evaluated from the CV curve.
- Figure 3.7 (a) GCD curves; (b) Calculated specific capacitance; and (c) Calculated specific capacity of NiS nanosheets, evaluated at various current densities.
- Figure 3.8 (a) Cyclic stability and capacity retention of NiS nanosheets analyzed from GCD at current density of 2A/g for 2500 cycles. (b) EIS spectra of NiS nanosheets electrode. (c)FESEM image and (d) EDS of NiS nanosheets electrode after cyclic stability for 2500 cycles
- Figure 3.9 (a) Open circuit potential; (b) Tafel Plots; and (c) Corrosion rate of Bare Ni foam and NiS nanosheets electrode after 0, 50, 200 and 400 GCD cycles.

LIST OF TABLES

| | |
|-----------|--|
| Table 1.1 | Comparison of Li-ion batteries and supercapacitors |
| Table 1.2 | Literature review of supercapatteries |
| Table 3.1 | Calculated C and C_s values from GCD curves |
| Table 3.2 | Corrosion study results |

NOMENCLATURE

| | |
|------------|--|
| i_p | Peak current |
| ν | Scan rate |
| C_s | Specific capacitance |
| C | Specific capacity |
| V | Potential at working electrode vs. reference electrode |
| d_{hkl} | Interplanar spacing on (hkl) plane |
| X | Adsorbed gas quantity |
| X_m | Monolayer adsorbed quantity |
| P | Equilibrium pressure |
| P_o | Saturation pressure |
| C | BET constant |
| i | Current |
| m | Mass of active material |
| E | Potential window in which potential is swept |
| Δt | Discharge time in GCD |
| R | Corrosion rate |
| M | Atomic weight of the metal |
| n | Number of electrons involved in the corrosion reaction |
| F | Faraday's constant |
| ρ | Density of metal |
| R_s | Solution resistance |
| R_{CT} | Charge transfer resistance |
| Q | Constant phase element |
| W | Warburg's impedance |

ACRONYMS

| | |
|---------|---|
| FESEM | Field effect scanning electron microscope |
| XRD | X-ray diffraction |
| XPS | X-ray photoelectron spectroscopy |
| EDS | Energy-dispersive X-ray spectroscopy |
| BET | Brunauer-Emmett-Teller |
| BJH | Barrett-Joyner-Halenda |
| EIS | Electrochemical Impedance Spectroscopy |
| OCP | Open circuit potential |
| LSV | Linear Sweep Voltammetry |
| EDLC | Electric double-layer capacitance |
| rGO | Reduced Graphene Oxide |
| AC | Activated Carbon |
| SA | Surface area of the sample |
| CSA | Cross-sectional area of adsorbate |
| mmpy | millimeters per year |
| SCE | Saturated Calomel Electrode |
| NiS/NiF | Nickel sulfide on Nickel foam |

CHAPTER 1

INTRODUCTION

1.1 Need for Energy Storage

Energy is required for every human activity. Humans learned a long time ago to convert different forms of energy to useful forms of energy. In current perspectives, the amount of energy produced is not always in sync with energy demand. Sometimes, the energy produced is more than demand, and at other times, demand is more than production. Therefore, energy storage is required to cover this gap, i.e., whenever surplus energy is there, it is stored and delivered at times of higher demands.

Most of the energy needs of humans are still covered by fossil fuels, which have several hazardous effects on the environment [1]. As a result, efforts are being made to increase the share of renewable energy in total energy production. Nevertheless, the challenge with most renewable energy sources is that they are intermittent sources of energy. For example, solar energy is available only in the daytime, and wind energy is available only in certain parts of the year (3-4 months). So, to ensure a continuous power supply, we need energy storage.

Energy can be stored in different forms- namely electrochemically [2], mechanically [3], electrically [4], or thermally [5]. Electrochemically, energy is stored in chemical energy and converted into electrical energy. These include batteries and supercapacitors. Mechanically, energy can be stored in the flywheels or through compressed air. Electrically, energy is stored through capacitors or superconducting magnets. Thermal energy is stored through hot water, hot fluid, or ceramic thermal storage.

1.2 What is a capacitor?

A capacitor is an electrical component with two terminals that stores energy in an electric field [6]. It consists of two parallel conductive plates, and in between is a dielectric. When we apply a potential across plates, the plates get oppositely charged, i.e., one gets positively charged, and the other gets negatively charged. In this way, the charges are stored, and to use it, we have to put a load across it.

1.3 What is a supercapacitor?

A supercapacitor is an electrochemical capacitor with a higher energy density than an electrolytic capacitor and a higher power density than Li-ion batteries. [Fig. 1.1](#)

shows the construction of the supercapacitor. Whenever a potential is applied across the electrodes, they get oppositely charged. These charged electrodes attract ions from the electrolyte, and hence, a layer is formed at the interface. This layer is known as the Helmholtz double-layer [7]. In this way, the charge is stored.

Other than electrodes, the separator and the electrolyte are essential components of a supercapacitor. A separator is a porous material used to prevent the shorting of electrodes. Since it is porous, it allows the ions to pass through itself [8]. The next thing is the electrolyte, which provides the ions. There are mainly three kinds of electrolytes- aqueous, organic, and ionic liquids [9]. Aqueous electrolytes have fast ionic diffusions, and also, they are cheap. However, the problem with them is the limited voltage window, i.e., these cannot be used above 1.23 V as the electrolysis of water starts at this value. Organic electrolytes can be used up to 3V, but they are costly, and there is always a chance of moisture getting in them, which deteriorates the working. Ionic liquids have a very high stable potential window of around 4.5 to 5V, thus giving high energy density. Nevertheless, ion diffusion in ionic liquids is very slow, resulting in poor power characteristics.

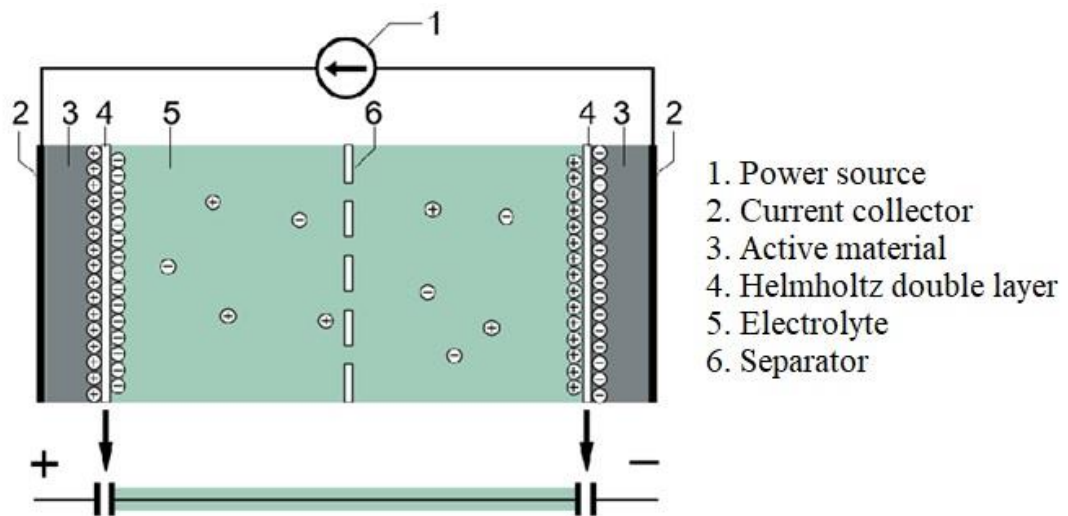


Figure 1.1 Typical construction of a supercapacitor

1.4 Types of Supercapacitors:

There are mainly three kinds of ultracapacitors [10]. These are:

- a. *Electric Double Layer Capacitors*: These are also known as EDLCs. These supercapacitors have a very high specific surface area and store charge only in the Helmholtz layer. Primarily carbon-based materials like activated carbon, graphene, carbon nanotubes, etc., are used in EDLCs.
- b. *Pseudocapacitors*: These supercapacitors store charge faradaically, which means some charge transfer will happen across the interface. Here charge storage occurs through fast surface redox reactions and the double layer. For pseudocapacitance, oxides of transition metals or conducting polymers are generally employed as electrode materials. These materials show very high specific capacitance (C_s), but their power density is compromised due to the slow kinetics of the redox processes. Also, conducting polymers have a problem with swelling and shrinkage while charging and discharging. This results in poor cyclic stability.
- c. *Hybrid capacitors*: These capacitors use both EDLC and pseudocapacitive materials resulting in higher energy density without much compromise in the power density.

1.5 Comparison of Supercapacitors and Batteries:

Table 1.1 Comparison of Li-ion batteries and supercapacitors

| Function | Li-ion battery | Supercapacitor |
|----------------------------|------------------|---------------------------------|
| Charge time | 10 min to 1 hour | 1-10 seconds |
| Cycle life (No. of cycles) | >500 | 1 million or 30000 hours |
| Cell voltage (V) | 3.6 to 3.7 | 2.3 to 2.75 |
| Specific power (W/Kg) | 1000 to 3000 | Up to 10000 |
| Specific energy (Wh/Kg) | 100 to 200 | 5 to 10 |
| Service life | 5 to 10 years | 10 to 15 years |

Batteries store charge via faradaic processes where ions intercalate and diffuse deep into the electrode structure. Supercapacitors store charge in the Helmholtz layer

or through fast surface redox reactions. This allows batteries to have superior energy density and supercapacitors to have better power density. However, it also causes batteries to have poor power density and supercapacitors to lack energy density. A brief comparison of batteries and supercapacitors is tabulated in Table 1.1 [11]. Supercapattery is a term used for devices that are hybrids of batteries and supercapacitors. These devices have both a superior energy and power density [12].

1.6 Literature Review

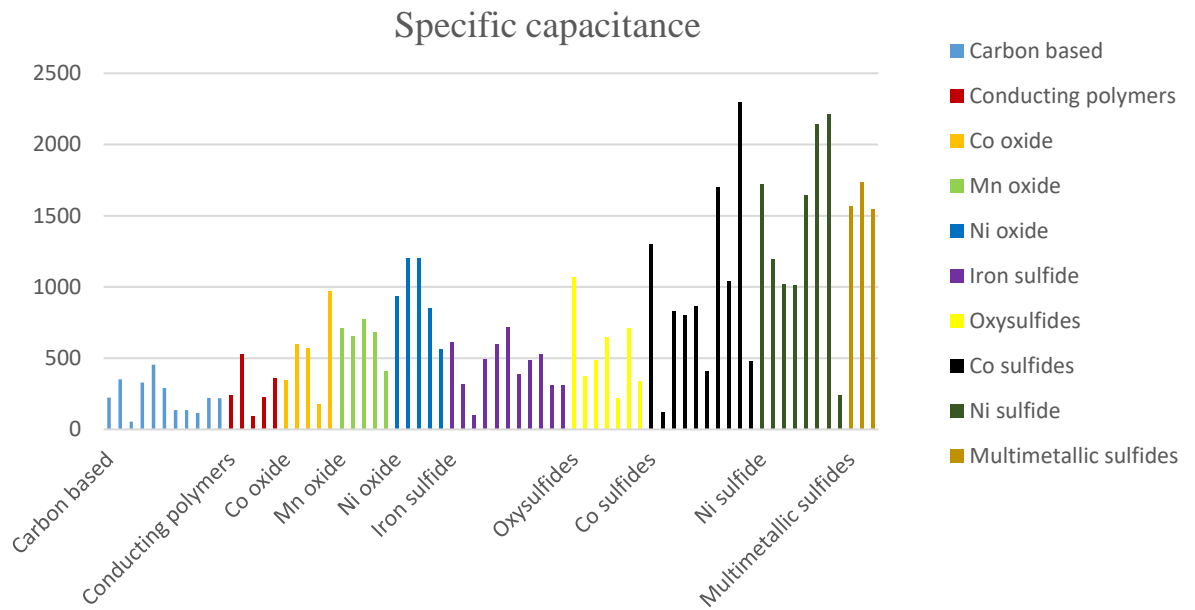


Figure 1.2 Specific capacitance of different materials

Many efforts are being made to enhance the energy and power density and cyclic stability of supercapacitors. Various electrode materials have been tried for supercapacitor applications. Fig. 1.2 shows the C_s values of different materials. Firstly, carbon-based materials were explored with limited specific capacitance because of EDLC behavior only [13]. They typically offer C_s in the range of 100-500 F/g. Then the oxides of various transition metals (such as Co, Mn, Ni, etc.) show higher specific capacitance values of around 500 to 1000F/g [14]. Oxysulfides of different materials have also been tried and showed specific capacitance values of more than 1000 F/g [15-19]. Sulfides of Fe, Co, and Ni have also been reported in the literature [20-21]. Cobalt and Nickel Sulfides have shown the best specific capacitance values (even more than

2000 F/g) [22,23]. There is an increase in multimetallic sulfides, and they also showed promising results of about 1300 to 1600 F/g. Sulfides of transition materials show excellent results because they have multiple possible stoichiometric compositions, crystal structures, valence states, and morphologies. Also, sulfides, in general, have better conductivity than oxides. Supercapatteries have also gained much interest in recent years. The following table 1.2 shows some of the most important works reported for supercapatteries:

Table 1.2 Literature review of supercapatteries

| S. N. | Material | Electrolyte used | Specific capacity | Energy density (Wh/kg) | Cyclic ability (retention) | Ref. |
|-------|--|------------------|-------------------|------------------------|----------------------------|------|
| 1 | Mesoporous Cobalt molybdate | 6M KOH | 64 C/g | 18.89 | 93% after 5,000 cycles | [24] |
| 2 | Co ₃ O ₄ /Au@MWCNT | 1M KOH | | 18.8 | 91.9% after 3,500 cycles | [25] |
| 3 | NiO/In ₂ O ₃ | 3M KOH | 101 C/g | 26.24 | 79% after 50,000 cycles | [26] |
| 4 | Co ₃ (PO ₄) ₂ ·8H ₂ O | 1M NaOH | | 29.29 | 77.9% after 1,000 cycles | [27] |
| 5 | NiCoP/NiF | KOH | 166 C/g | 36 | 80% after 25,000 cycles | [28] |
| 6 | Ni ₃ (PO ₄) ₂ ·8H ₂ O | 1M NaOH | 67.4 mAh/g | 33.4 | 89% after 10,000 cycles | [29] |
| 7 | Ni-Co-Mn-OH | 6M KOH | 206 C/g | 42.8 | 90.2% after 5,000 cycles | [30] |
| 8 | MnO ₂ @CoS | 3M KOH | 147 C/g | 34.72 | 89.6% after 9,000 cycles | [31] |
| 9 | rGO/TiO ₂ //AC | 1M KOH | 120 C/g | 54.37 | 92% after 3,000 cycles | [32] |

1.7 Research Gaps:

Although much attention has been given to studying and engineering the electrodes for electrochemical energy storage devices, some gaps remain in the literature. Some of these are listed below:

1. Enhanced interlayer spacing: There is still a need to synthesize material with more surface area accessible for electrolytes and thus increase the specific capacitance.

2. Explore metal sulfides which have the potential to give more active surface sites.
3. Find materials that are structurally stable even after intercalation and de-intercalation of ions.

1.8 Objectives:

In view of the above research gaps identified from the literature, we aimed for the following objectives for this thesis work.

1. To synthesize Nickel Sulfide with a morphology providing a high specific surface area.
2. To electrochemically characterize the Nickel Sulfide.
3. To study the cyclic stability of the synthesized electrode.
4. To study the corrosion behavior of NiS in electrolytes and correlate it with the cyclic stability of the electrode.

CHAPTER 2

EXPERIMENTAL SECTION

2.1 Synthesis of Nickel Sulfide

NiS nanosheets were synthesized via the facile hydrothermal method. In brief, nickel nitrate hexahydrate ($\text{Ni}(\text{NO}_3)_2 \cdot 6\text{H}_2\text{O}$, 99.99%) and thiourea ($\text{CH}_4\text{N}_2\text{S}$, 99.99%) in the equimolar ratio were dissolved independently in 10ml of DI water under vigorous stirring and mixed. Then, Methylamine is added to the above solution. It is stirred for 30 minutes. Methylamine acts as a stabilizer and forms a complex $[\text{Ni}(\text{MeNH}_2)_2]^{2+}$, which slows down the reaction with thiourea and promotes the growth of a large number of nucleation sites. Subsequently, the above solution was sealed in a 25 ml Teflon-lined stainless-steel autoclave for 18h at 150 °C (heating rate: 5 °C.min⁻¹) under auto-generated pressure and allowed to be cooled at room temperature. The final NiS product was centrifuged and washed with DI water and ethanol, followed by drying at 60 °C for two hours to obtain the black powder of NiS nanosheets.

2.2 Characterization Techniques

2.2.1 Field Emission Scanning Electron Microscopy

It is a characterization technique that produces the image of a sample by scanning an electron beam on its surface. The electron beam has a far better resolution than visible light because its wavelength can be 10⁵ times smaller than visible light. Unlike conventional scanning electron microscopes, which generate electron beams using thermionic emission, FESEM uses a strong electric field (field emission guns) to generate electron beams. This electron beam is accelerated through a high electric potential (several kilovolts), and then with the help of magnetic lenses and deflection coils, it is made to focus and scan the sample. When this electron beam strikes the sample, it generates X-rays, backscattered electrons, auger electrons, and secondary electrons. These are detected by a detector that converts them into an electric signal further displayed on a computer. Morphological features of the sample were examined using FESEM, JEOL JSM-6500F.

2.2.2 Energy Dispersive X-Ray Spectroscopy (EDS)

It is an X-Ray technique for determining elements present in the synthesized samples. As the electron beam hits any inner shell electron of the analyte, the electron is knocked off. This creates a hole in the atom's inner shell, which is filled by one of

the electrons from the outer shells. When electrons move from higher energy to lower energy shells, it emits X-Rays. The energy of these X-rays is unique to the element and transition. Hence, detecting these X-rays gives the elemental makeup of the sample. EDX of the sample was recorded using the Oxford EDS X-MAX 20 mm.

2.2.3 X-Ray Diffraction

The crystallinity of a sample can be determined using XRD. Crystal structures function as diffraction grating for X-rays because the order of interplanar spacing in crystal structures is the same as the wavelength of X-rays. It is based on Bragg's law which gives the relation between wavelength of incident x-ray (λ), interplanar spacing (d_{hkl}), and angle of incidence (θ). Mathematically,

$$N * \lambda = 2d_{hkl} \sin(\theta) \quad (2.1)$$

In XRD, the sample is irradiated with x-rays, and after interacting with the sample, the intensity at different angles is recorded. XRD is primarily used to know the crystal structure of the sample. It can also be used to get the quantitative phase analysis, crystallite size, microstructure strain, etc. XRD was recorded using XRD, Empyrean, PANalytical, Cu-K α , $\lambda=1.5406 \text{ \AA}$.

2.2.4 X-ray photoelectron spectroscopy (XPS)

XPS determines the chemistry of a sample's surface. X-ray beam is irradiated on the solid sample surface to get the XPS spectra. These X-rays provide enough energy for the electrons to be ejected from the top surface (1-10 nm) of the sample. The ejected electrons kinetic energy and the number of electrons are recorded. Since electrons in different shells and subshells (s, p, d, etc.) have different energies, this spectrum can be used to know the elemental composition of the sample. XPS measurement was carried out on Thermo Scientific XPS using monochromated Al K α X-rays.

2.2.5 BET surface area analysis

BET analysis directly measures the sample's surface area and pore size distribution. It is founded on the principles of adsorption and desorption of gas molecules on the sample's surface. Firstly, the sample is entirely degassed by putting it in a vacuum and temperature for extended times. After that, an inert gas such as Nitrogen is made to flow over the sample. Isolated sites begin to adsorb gas molecules

at low pressures at the sample surface. As the pressure increases, monolayer forms. BET equation is given as [33]:

$$\frac{1}{X\left(1-\frac{P}{P_0}\right)} = \frac{C-1}{Xm.C} \left(\frac{P}{P_0}\right) + \frac{1}{Xm.C} \quad (2.2)$$

This equation gives a linear relation between $\frac{1}{X\left(1-\frac{P}{P_0}\right)}$ and $\frac{P}{P_0}$. The following equation can then calculate the surface area of the sample [34]:

$$SA = \frac{1}{\text{slope} + \text{intercept}} \cdot CSA \quad (2.3)$$

As the pressure increases, multilayers start forming, and all pores in the sample get filled. BJH distribution can be used to calculate pore diameter, volume, and distribution. BET analysis was done in an automated gas sorption analyzer (Quantchrome Autosorb iQ2).

2.3 Electrochemical Characterization

In electrochemical characterization, potential, charge, and current are measured to characterize the electrode. To characterize any electrode, we must measure the potential across it and the current passing through it. It can be done either in two- or three- electrode configurations. Two electrode configuration comprises a working electrode and a counter electrode. The counter electrode in a two-electrode setup serves both purposes. First, it completes the circuit and allows charges to flow in the circuit, and second, it maintains constant interfacial potential regardless of current value. However, practically, no electrode can fulfill both these conditions. This is why a three-electrode configuration uses different electrodes for these functions: a counter electrode and a reference electrode [35]. The reference electrode is used to measure and control potential at the working electrode. Since the negligible current is passed through it, the iR drop between the reference and working electrode is minimal. As a result, the potential at the working electrode is much more stable, giving more control over the working electrode potential. Widely used reference electrodes are Standard Calomel Electrode and Ag/AgCl electrodes.

Various techniques to characterize the energy storage of supercapattery materials are as follows:

2.3.1 Cyclic Voltammetry (CV)

It is a technique in which the potential at the working electrode is increased linearly with time up to a specific potential, and once a particular potential is reached, it is decreased linearly to come back to the initial potential, and the current is recorded vs. the potential applied at the working electrode. The rate at which the voltage is ramped is known as the scan rate. Many qualitative and quantitative data can be extracted from the cyclic voltammetry curves. Just by looking at the curves, one can tell whether it is a supercapacitor, pseudocapacitor, or a battery type of curve. It is shown in Fig. 2.1 [36].

EDLC materials typically show a rectangular CV curve, whereas pseudocapacitive materials show a broad oxidation and reduction hump at the same potential, and the battery-type materials show sharp reduction and oxidation peaks at different potentials. Cyclic voltammetry can also be used to measure the specific capacitance of the material. Specific capacitance from CV is given by [37]:

$$C_s = \frac{\int_{V_1}^{V_2} i dV}{mEv} \quad (2.4)$$

Where, $\int_{V_1}^{V_2} i dV$ is the area under the CV curve from potential V_1 to V_2 , m is the mass of electrode (g), E is the potential window ($=V_1-V_2$) (V), and v is the scan rate (V/s).

Cyclic voltammetry is generally done at different scan rates. This can be used to know the mechanism for charge storage on the electrode. The current response of the electrode at any scan rate can be construed as the summation of two processes: first is the slow diffusion-controlled process (i_{diff}), and the second is the fast surface process, such as charging the double layer at the electrode surface or initiating the surface redox reactions (i_{cap}). This can be written as [38]:

$$i = i_{cap} + i_{diff} = av^b \quad (2.5)$$

$$\log I = \log a + b \log v \quad (2.6)$$

where a and b are constants.

When the b value is near 1, it shows the contribution is majorly from rapid near-surface faradaic reactions and EDLC behavior, whereas if the value of b is near 0.5, it signifies that the significant contribution is from the diffusion-controlled process as in batteries.

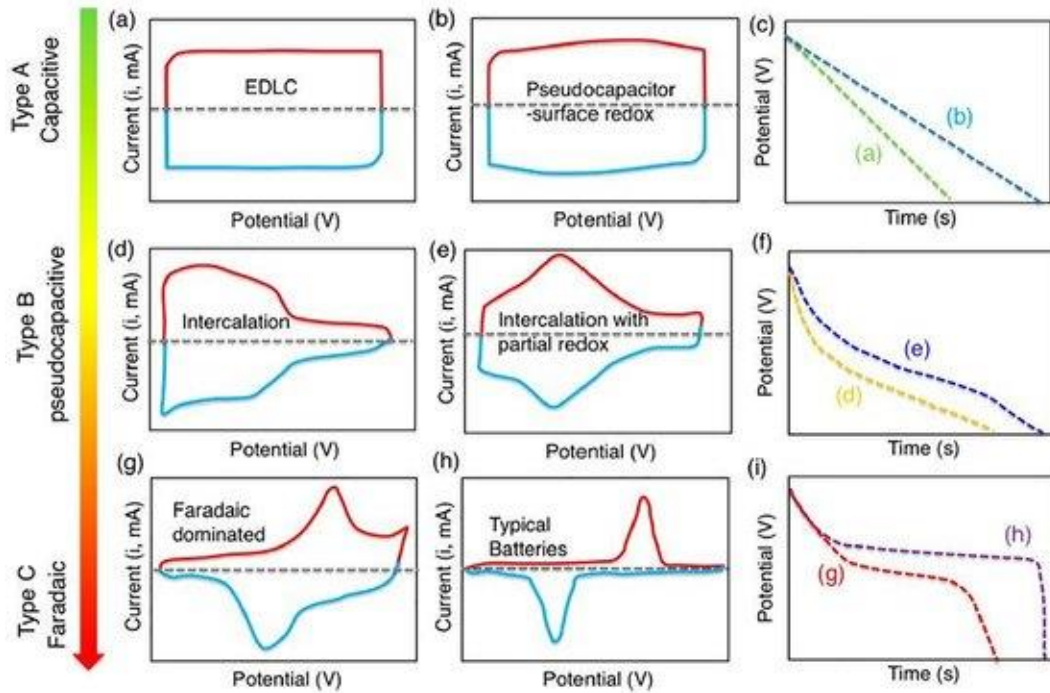


Figure 2.1 Cyclic voltammety (a,b,d,e,g,h) and their corresponding GCD curves for different types of energy storage materials [36]

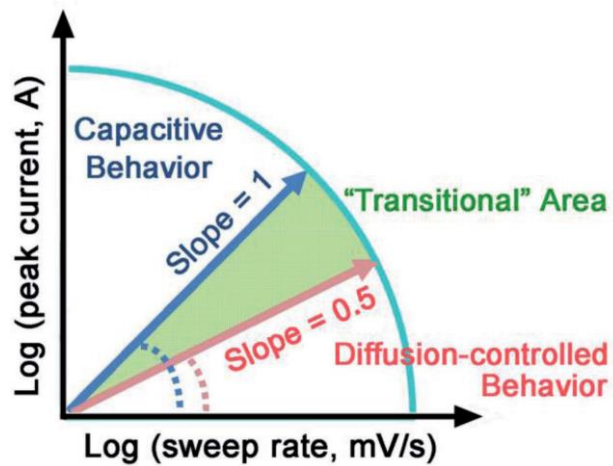


Figure 2.2 Significance of slope of $\text{Log}(i_p)$ vs. $\text{log}(\text{sweep rate})$ for determining behavior of electrode [38]

2.3.2 Galvanostatic charge-discharge:

In this technique, the electrode is continuously charged and discharged by applying a constant current, while the potential is measured with respect to time. Like cyclic voltammetry, this can also be used to know the nature of reactions happening at the electrode surface. If the potential varies linearly and a triangular shape is seen, it signifies fast surface redox reactions or the double-layer behavior. However, the plateau observed signifies slow diffusion-controlled behavior. Further, it can also be used to get quantitative data, such as calculating specific capacitance (C_s) and specific capacity (C). Specific capacitance is given as [37]:

$$C_s = \frac{I}{m} \int_{V_1}^{V_2} \frac{1}{V} dt \quad (2.7)$$

Specific capacity is calculated as:

$$C = \frac{I\Delta t}{m \cdot 3.6} \quad (2.8)$$

2.3.3 Electrochemical Impedance Spectroscopy:

EIS is used to characterize the impedance characteristics of an electrode. It can deconvolute different complex processes into a series of simple electrochemical processes [39]. In EIS, AC signal with a small amplitude is applied, and the corresponding impedance is measured. The impedance data thus obtained can be fitted to the simulated response of any circuit, and thus various processes can be known. We generally get two plots through EIS: the Bode plot and the Nyquist plot. Bode plot is a plot between the phase angle and frequency, whereas the Nyquist plot is the plot between the complex and real parts of the impedance. Generally, an AC signal is applied from 10 mHz to 100,000 Hz for electrochemical energy storage devices. The Nyquist plot consists of three parts for such systems: a semi-circular curve in high-frequency, a line with a slope of about 45° in the mid-frequency, and a line with a high slope in the low-frequency range [35]. Semicircle is a little offset from the origin. The point at which the semicircle starts from the real axis is the value of equivalent series resistance, which can be used to calculate the power density of the electrode or device. The diameter of the semicircle gives the charge transfer resistance. The line with a

slope of about 45° is due to Warburg impedance, and then there is a line with a slope of about 90° , which signifies the capacitive behavior.

All these electrochemical measurements were done using a three-electrode configuration. The electrodes were prepared by a simple drop-casting process. Typically, a substantial amount of NiS sample was mixed with a binder (Nafion) in ethanol and drop cast on NiF ($1\text{cm} \times 1\text{cm}$). The mass loading was ~ 2 mg. The electrochemical measurements of as-prepared electrodes were evaluated in 1M KOH on an electrochemical workstation (Autolab, PGSTAT204, Metrohm) using a three-electrode configuration. Platinum wire as a counter electrode and SCE as a reference electrode were used.

2.4 Corrosion studies

Corrosion is the deterioration of material properties of any material owing to the chemical or electrochemical processes occurring at the material surface/surrounding interface. Generally, corrosion is a process in which a metal is converted to its more chemically stable naturally occurring oxide. Weight loss measurements are the best way to study corrosion. However, these tests are prolonged since, generally, corrosion rates are in the order of a few mmpy (millimeter per year). Another way to perform corrosion studies is through electrochemical measurements. Some of the advantages of electrochemical corrosion testing are that it is fast, sensitive, and can be used either in the lab or in the field.

Various techniques to do electrochemical corrosion testing are:

2.4.1 OCP (Open Circuit Potential):

It is the potential existing between terminals in a cell when the circuit is open and no potential or current is applied across it. It is done to check whether the electrode has attained equilibrium with the electrolyte or not.

2.4.2 LSV (Linear Sweep Voltammetry):

In this method, the electrode potential is linearly increased from a value much lower than OCP to a value much higher than OCP, and the corresponding current is recorded. It can be used to get the Tafel plot which is further used to get E_{corr} , I_{corr} , and corrosion rates [40].

The corrosion rate of any material is given by:

$$R = \frac{M}{nF\rho A} i_{corr} \quad (2.9)$$

Corrosion studies were done on Autolab, PGSTAT204, Metrohm. OCP was carried out for 1800 seconds. Linear sweep voltammetry was done from -0.4V to 0.4V vs. SCE with a scan rate of 1.5 mV per second in a 1M KOH electrolyte medium.

CHAPTER 3

**RESULTS AND
DISCUSSION**

3.1 Material Characterization

3.1.1 Field Emission Scanning Electron Microscopy

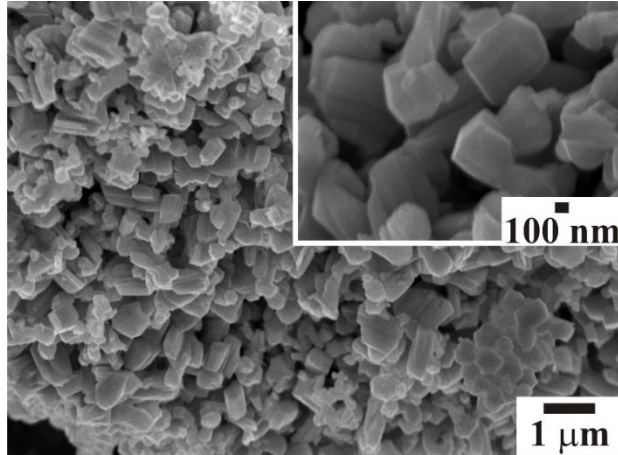


Figure 3.1 FESEM images of NiS nanosheets

Fig. 3.1 shows the FESEM images of the synthesized Nickel Sulfide. The low magnification FESEM image represents the uniformly distributed growth of NiS nanoparticles. However, a high magnification image in the inset of Fig. 3.1 represents the growth of nanosheets like morphologies of Nickel Sulfide. In some places, several sheets have got stacked over one another. The size of nanosheets ranges from 300-700 nm, and their thickness ranges from 20-90 nm.

3.1.2 Energy dispersive X-Ray Spectroscopy

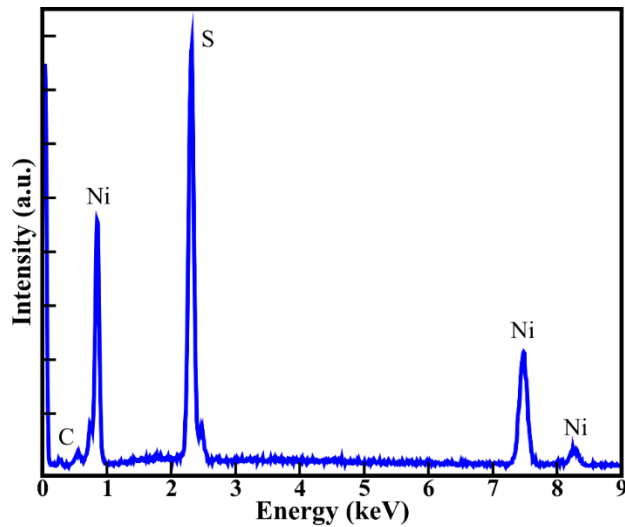


Figure 3.2 EDS spectra of as-synthesized NiS nanosheets

EDS was employed to know the elements present in the sample. Peaks were observed at the energy values of 0.85, 2.30, 7.47, and 8.26 keV. The peak at 2.30 keV is the characteristic peak of Sulfur. The rest three peaks are of Nickel. Hence, EDS shows the presence of Nickel Sulfide without any impurities.

3.1.3 X-ray Photoelectron Spectroscopy

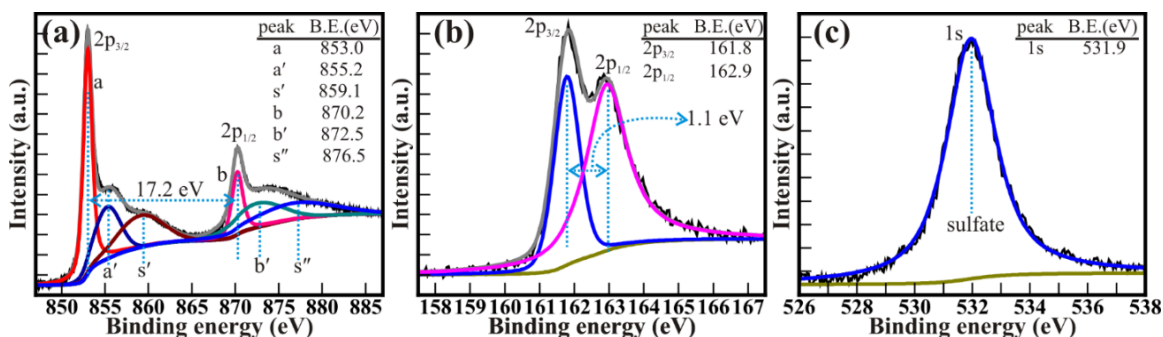


Figure 3.3 High-resolution XPS Spectra of (a) Ni(2p); (b) S(2p); and (c) O(1s) core levels of the NiS nanosheets. The XPS spectra were deconvoluted via the Voigt function using Shirley's background.

XPS was done to know the chemical composition and electronic states of Nickel Sulfide nanosheets. Fig. 3.3 shows the high-resolution XPS spectra of the Ni (2p), S(2p), and O(1s) core levels of Nickel Sulfide. Peaks in XPS spectra were deconvoluted using the Voigt curve fitting function, followed by Shirley background to know the double peak features of Ni(2p) and S(2p). The XPS spectra of Ni showed four peaks that, on deconvolution, fitted perfectly with six peaks identified as a, a', s', b, b', and s'' consecutively located at a binding energy of 853.0, 855.2, 859.1, 870.2, 872.5 and 876.5 eV, which are assigned to $\text{Ni}^{2+}(2p_{3/2})$, $\text{Ni}^{3+}(2p_{3/2})$, $\text{Ni}^{2+}(2p_{3/2})$ shakeup satellite peak, $\text{Ni}^{2+}(2p_{1/2})$, $\text{Ni}^{3+}(2p_{1/2})$ and $\text{Ni}^{2+}(2p_{1/2})$ shakeup satellite peaks, respectively. The distinctly intense peak of $\text{Ni}^{2+}(2p_{3/2})$ and $\text{Ni}^{2+}(2p_{1/2})$ core levels of Ni^{2+} ions evidenced the formation of NiS nanosheets. However, it is accompanied by other peaks of Ni^{3+} but its intensity compared to Ni^{2+} is much lesser, indicating its insignificance. The energy separation of $17.2 (\pm 0.2)$ eV between $\text{Ni}^{2+}(2p_{3/2})$ and $\text{Ni}^{2+}(2p_{1/2})$ core levels remained identical for their satellite peaks. XPS spectra of S showed two distinct peaks located at a binding energy of 161.8 and 162.9 eV are assigned to core levels of $\text{S}^{2-}(2p_{3/2})$ and $\text{S}^{2-}(2p_{1/2})$. Moreover, the deconvolution of O(1s) core level spectra indicates

the appearance of the peak at a binding energy of 531.9 eV is assigned to the sulfate and ruled out the formation of the oxidized phase at the surface. Overall, XPS analysis confirms the formation of pure stoichiometric NiS nanosheets without any oxidized phase.

3.1.4 X-Ray Diffraction

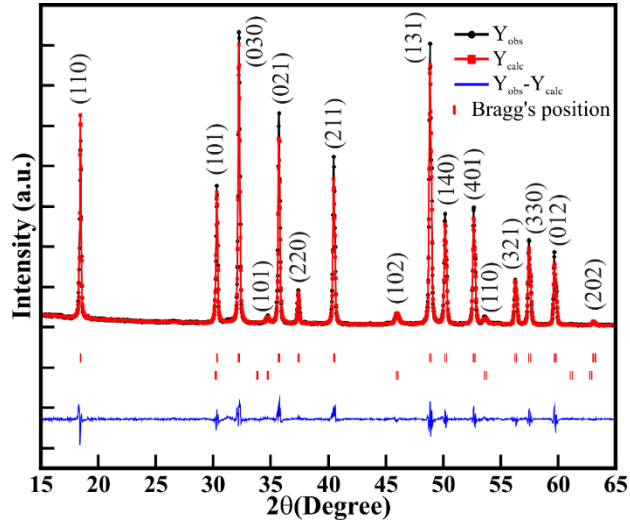


Figure 3.4 Rietveld refined XRD of NiS nanosheets along with residual curve located at the bottom

NiS is known to crystallize in two different phases, such as hexagonal α -NiS (nickeline phase) shows metal to semiconductor properties, and rhombohedral β -NiS (millerite phase), which exhibits metallic behavior [41]. All the XRD peaks of the NiS nanosheets shown in Fig. 3.4 can be indexed to the rhombohedral millerite structure with space group $R3m$, which matches with β -NiS (JCPDS card no. 65-3686). A small fraction of hexagonal α -NiS is formed as a secondary phase, corresponding to the hexagonal α -NiS phase (JCPDS card no. 75-0613). All peaks are distinct, and the peak at 30.34° is overlapping, which confirms the presence of mixed-phase α - β NiS. Rietveld refinement was used to examine the mixed-phase structure which leads to refined lattice parameters $a = b = 9.618 \text{ \AA}$ and $c = 3.152 \text{ \AA}$ for rhombohedral millerite phase and $a = b = 3.417 \text{ \AA}$ and $c = 5.298 \text{ \AA}$ for hexagonal with the space group of $P63/mmc$ with good fitting factors such as $R_{wp} = 13.4 \%$, $R_p = 12.5 \%$ and $R_B = 6.83 \%$

and $\chi^2 = 5.01$. The Millerite and Hexagonal phase fraction was calculated to be 96.97% and 3.03 %, respectively.

3.1.5 BET Surface area analysis

N₂ adsorption and desorption measurements were employed to examine the surface area and pore structure. As shown in Fig. 3.5(a), the isotherms of the NiS display adsorption-desorption curves, which corresponds to the H3 hysteresis loop [42], which establishes the mesoporous nature of the sample. The BET-specific surface area is 9.247 m²/g with a total pore volume of 0.046 cm³/g. Furthermore, the BJH pore size distribution of the NiS is displayed in Fig. 3.5 (b), which represents the pore diameter between 3 nm – 10 nm. Hence, the larger surface area, abundant channels, and smaller pore size offer highly accessible active sites for electrolyte ions, ensuring fast electron/mass transfer and providing the shortest pathways for charge transfer between electrode and electrolyte to improve the electrochemical energy storage property.

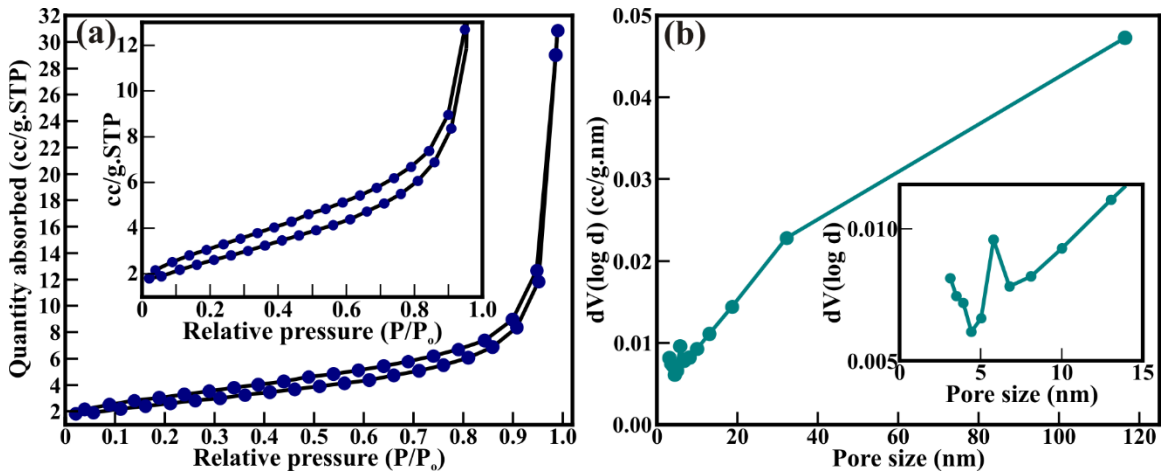


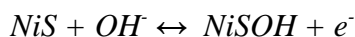
Figure 3.5 (a) N₂ adsorption-desorption isotherm, and (b) BJH pore size distribution of the NiS nanosheets

3.2 Electrochemical Characterization

NiS' electrochemical performance was investigated using the three-electrode cell with a 1M KOH aqueous alkaline electrolyte from 0 – 0.6 V (~ 2 mg/cm² mass loading).

3.2.1 Cyclic Voltammetry

Fig. 3.6 (a) shows the CV curves of NiS recorded at various scan rates from 1 – 10 mV/s. The reversible redox peaks from the CV curves are ascribed to the faradaic redox reactions between Ni^{2+} and Ni^{3+} as described by the following reaction [43]:



Furthermore, with increasing scan rate, the area enclosed within the curve increases as predicted by the Randles-Sevcik equation, and the symmetric and reversible shape of the CV curve as the scan rate is varied indicates the rapid charge transport at the electrode-electrolyte interface during surface redox reactions [44]. Moreover, the cathodic/anodic peak position shifts relatively at higher and lower potentials due to the inflow and outflow of OH^- ions. The large surface area of NiS perhaps provides numerous trap levels, where intercalation and de-intercalation of free electrons/ions enhance ionic conductivity and increase current. Moreover, the b value is 0.548 (± 0.025), and the peak currents of the CV redox peaks, as shown in Fig. 3.6(b), display the linear increment with $v^{1/2}$, which justifies the dominance of the battery type diffusion mechanism in NiS. Furthermore, the highest specific capacitance of NiS obtained from CV curves is 2138 F/g at 1 mV/s tends to reduce exponentially 774 F/g at a higher sweep rate of 10 mVs^{-1} as represented in Fig. 3.6 (c). Moreover, at higher sweep rates, the OH^- ions experience a barrier to diffuse through the surface, leading to sluggish kinetics.

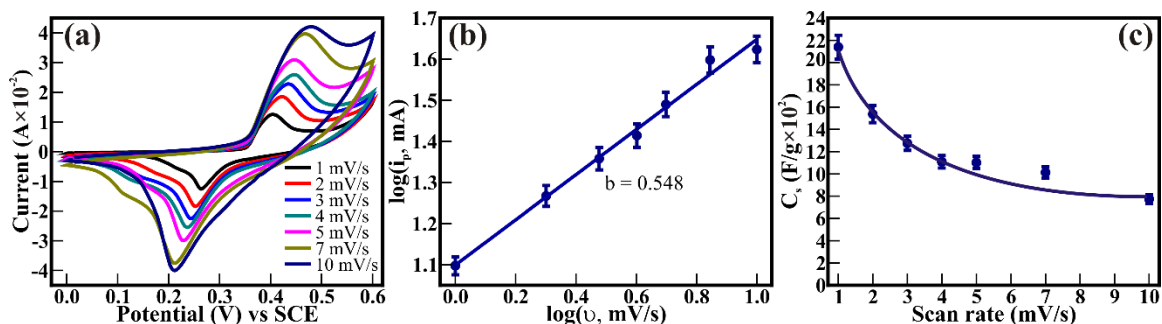


Figure 3.6 (a) Cyclic voltammograms of NiS nanosheets at various scan rates in 1M aq. KOH electrolyte. The graphical illustration of (b) log of peak current density (i_p) vs log of scan rate, and; (c) specific capacitance at various scan rates, evaluated from the CV curve.

3.2.2 Galvanostatic Charge Discharge

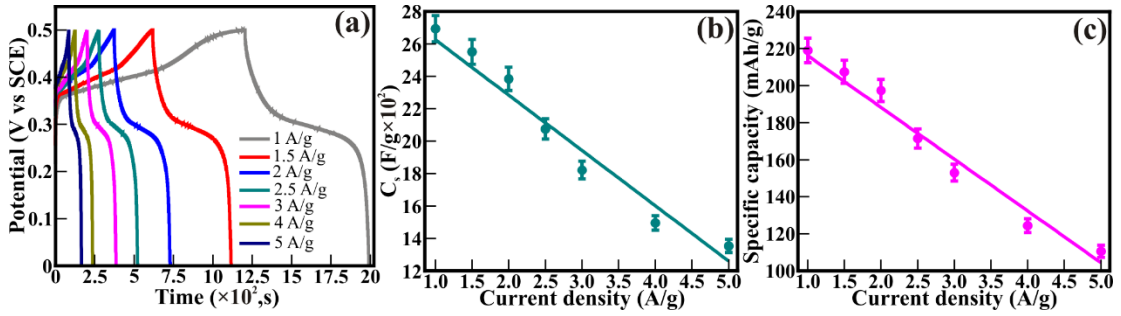


Figure 3.7 (a) GCD curves; (b) Calculated specific capacitance; and (c) Calculated specific capacity of NiS nanosheets, evaluated at various current densities.

The GCD studies of NiS were performed to understand the effect of different current densities on the electrochemical energy storage performance. Fig. 3.7(a) demonstrates the GCD curves of NiS at different current densities. The presence of plateaus at around 0.38 V for charging and around 0.3V during discharging also shows that the electrode is a battery-type electrode. This is also in line with the results of cyclic voltammetry. The maximum C_s and C were found at 1 A/g, and the value calculated was 2693 F/g and 219 mAh/g. With increasing current density, both the C_s and C decrease. This is shown in fig 3.6(c). The lowest calculated values were at 5A/g, and the C_s and C were 1353 F/g and 110.5 mAh/g. The reason for this decline is that at higher current densities, the ions within the electrolyte do not get enough time to diffuse into the electrode. Hence, all the possible sites are not utilized, and thus, the charge stored is less. Table 3.1 shows the calculated C and C_s values at different scan rates.

Table 3.1 Calculated C and C_s values from GCD curves

| Current density (A/g) | 1 | 1.5 | 2 | 2.5 | 3 | 4 | 5 |
|-----------------------|--------|--------|--------|--------|--------|--------|--------|
| C (mAh/g) | 219.1 | 207.5 | 197.4 | 171.5 | 153.0 | 124.5 | 110.5 |
| C_s (F/g) | 2693.7 | 2550.9 | 2383.9 | 2074.8 | 1820.5 | 1495.2 | 1353.1 |

3.2.3 Cyclic stability and EIS

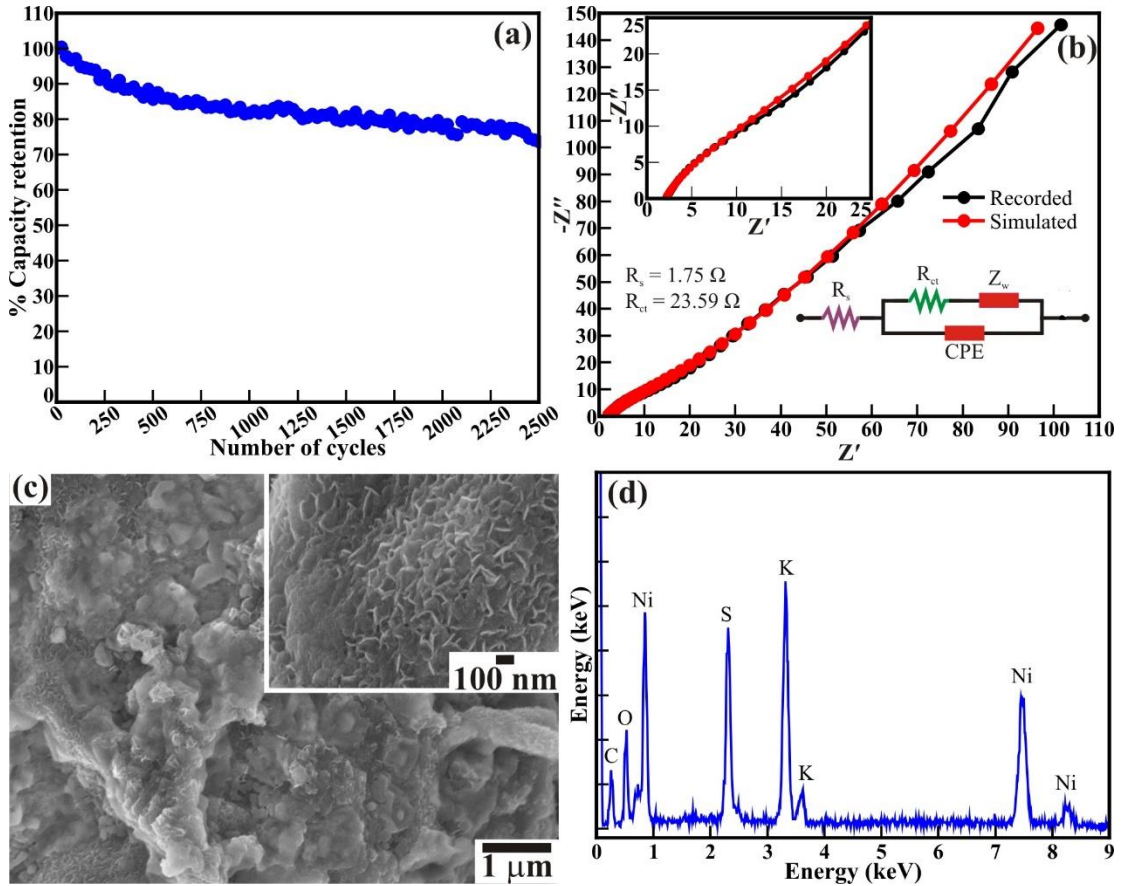


Figure 3.8 (a) Cyclic stability and capacity retention of NiS nanosheets analyzed from GCD at current density of 2A/g for 2500 cycles. (b) Electrochemical Impedance Spectra of NiS nanosheets electrode. Inset shows the equivalent circuit used for fitting EIS spectra. (c) FESEM image and (d) EDS of NiS nanosheets electrode after cyclic stability for 2500 cycles

Further, the cyclic stability of the electrode was tested for 2,500 cycles. The gradual decrease in C_s is observed with the increase in the number of cycles, as shown in Fig. 3.8 (a). After 2,500 cycles, the C_s retained was 73.6 % of the initial value. Fig. 3.8 (c) shows the SEM image of the electrode after 2,500 cycles. It is observed that the diffusion of OH^- ions has partially affected the morphology of NiS nanosheets. The initially present nanosheets were fused together, reducing the surface area. Fig. 3.8(d) shows the EDS of the electrode after 2,500 cycles. It shows that K^+ ions and OH^- ions

have diffused inside the electrode and have not come out even after discharge. This also contributes to the reduced performance of the electrode.

EIS was employed to learn about the reaction kinetics at the electrode-electrolyte interface. Fig. 3.8 (b) represents the Nyquist plot of the Nickel Sulfide electrode. The plot shows a semi-circular region at the high frequencies and a straight line with a higher slope at the low-frequency region. The inset figure shows the equivalent circuit model for fitting the spectra in which R_s is the bulk solution resistance, R_{CT} is the charge transfer resistance, Q is the constant phase element formed between electrode and electrolyte, W is the Warburg impedance, and C is the faradaic pseudocapacitance. R_s is the intercept of the plot with the real axis, representing the resistance of solution and contact resistance between the current collector and active material. Fitted data gives the R_s and R_{ct} values of 1.75 (± 0.295) and 23.59 (± 3.21) ohm, respectively. The smaller semicircle diameter in the Nyquist plot shows that charge transfer resistance is low, and the steep straight line shows that the diffusion resistance is also low.

3.3 Corrosion Studies

Corrosion studies were done alongside cyclic stability tests to study the deterioration of Nickel Sulfide nanosheets in KOH electrolyte. Fig. 3.9(a) shows the open circuit potentials of bare Ni foam and NiS/NiF initially and after 50, 200, and 400 cycles. It shows that initially, the OCP increases as the number of charge-discharge cycles increases, but after 200 cycles, it becomes almost constant. This shows that the electrode is more prone to corrosion initially, but after almost 200 cycles, the tendency to corrode becomes almost constant. Fig. 3.9(b) shows the polarization curves of the Ni foam and NiS/NiF. The same trend as that of OCP can also be observed in this plot. As the number of charge-discharge cycles increases, E_{corr} first increases and becomes constant. This result is also in line with the observations of OCP. Calculated values of corrosion parameters are given in table 3.2.

Fig. 3.9(c) shows a clear trend between the number of charge-discharge cycles and the corrosion rate. Initially, the corrosion rate was very high, but it kept decreasing. After almost 200 cycles, the corrosion rate becomes almost constant. A similar trend can be seen in the cyclic stability curve shown in fig. 3.8(a) also, where the decrease in

capacity at the initial cycles is very sharp, but after a few hundred cycles, the decline is almost constant.

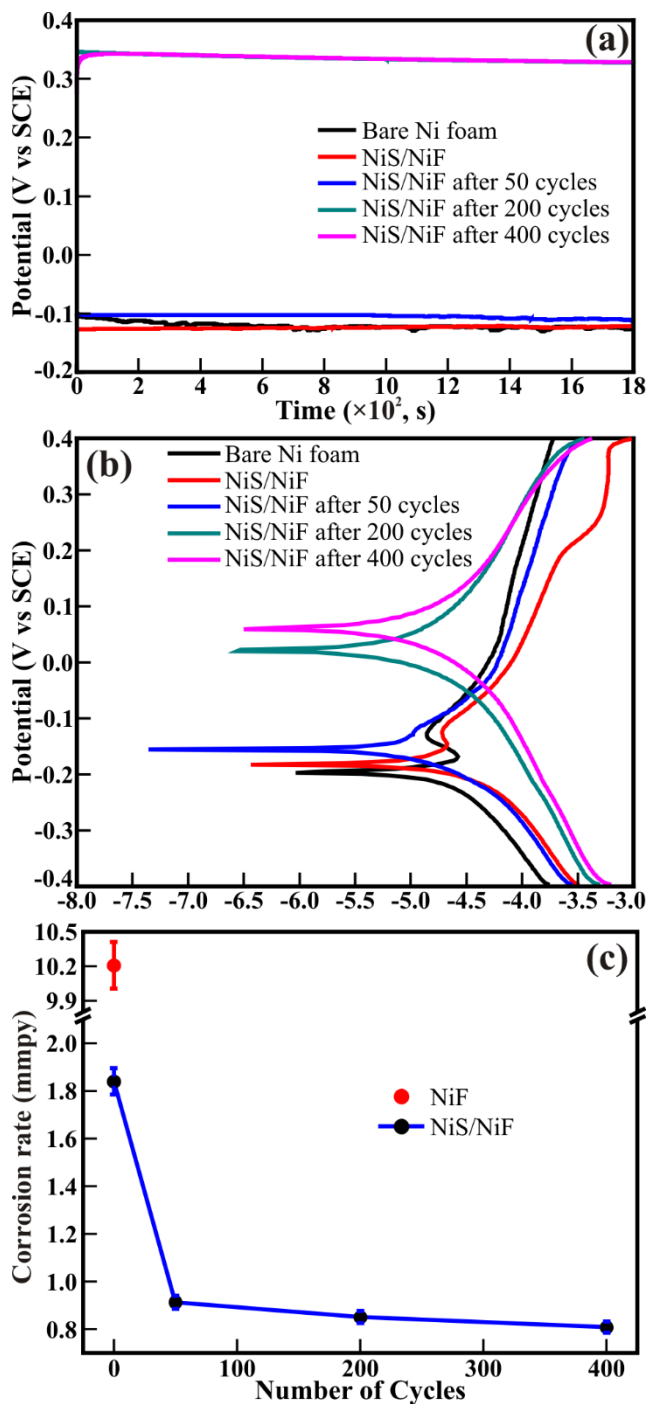


Figure 3.9 (a) Open circuit potential; (b) Tafel Plots; and (c) Corrosion rate of Bare Ni foam and NiS nanosheets electrode after 0, 50, 200 and 400 GCD cycles.

Table 3.2 Corrosion study results of NiS nanosheets

| Material | E_{corr} (V) | I_{corr} (mA) | Corrosion rate (mmpy) |
|--------------------------|-----------------------|------------------------|-----------------------|
| Ni Foam | -0.194 | 47.8 | 10.2094 |
| NiS/NiF | -0.181 | 72.8 | 1.84 |
| NiS/NiF after 50 cycles | -0.155 | 36.1 | 0.913 |
| NiS/NiF after 200 cycles | 0.0215 | 33.6 | 0.850 |
| NiS/NiF after 400 cycles | 0.0603 | 31.96 | 0.808 |

CHAPTER 4:

**CONCLUSIONS
AND FUTURE
SCOPE**

4.1 Conclusions

In conclusion, we have synthesized Nickel Sulfide through the hydrothermal method. The morphology obtained after optimization of reaction parameters is nanosheets. The size of these nanosheets was 300 to 700 nm, and their thickness ranged from 20 to 90 nm. EDS verified the presence of Ni and S only in the sample. Further XPS confirmed the formation of NiS, and no presence of any other sulfide such as NiS₂ or Ni₃S₂ was detected. XRD confirmed the crystallinity of the sample, and XRD matched with the JCPDS Card no. 65-3686, showing the formation of the millerite phase. A small impurity phase of the hexagonal phase is also present, which matches with the JCPDS Card no. 75-0613. Rietveld refinement was used for quantitative analysis and showed that millerite and hexagonal phases are present in the ratio of 96.97% and 3.03%, respectively. Three-electrode configuration was employed to conduct electrochemical measurements to study the charge storage characteristics of the synthesized Nickel Sulfide. Cyclic voltammetry showed sharp oxidation and reduction peaks, indicating battery-type behavior. Galvanostatic charge-discharge was used to calculate the electrode's C and C_s. It showed a maximum C of 219 mAh/g and a C_s of 2693 F/g at 1 A/g. It also showed excellent cyclic stability. Even after 2,500 cycles, it retained 73.6 % of its capacity. EIS was done to study the electrode processes and showed low charge transfer and diffusion resistance. Corrosion studies were also done along with cyclic stability, which showed that the corrosion rate first decreases and becomes almost constant after 200 cycles. Hence, we can conclude that Nickel Sulfide is an up-and-coming candidate for high-capacity supercapattery.

4.2 Future scope

There are still many unexplored territories to reach the full potential of Nickel Sulfide. Organic electrolytes and ionic liquids should be explored to get a wider potential window and higher energy density. Further, binder-free electrodes can also be made by growing Nickel Sulfide directly on the current collector. Moreover, multimetallic sulfides, including Nickel and composites, can further improve the charge storage characteristics of supercapattery.

REFERENCES

1. Abbasi, K. R., Shahbaz, M., Zhang, J., Irfan, M., & Lv, K. (2022). Analyze the environmental sustainability factors of China: The role of fossil fuel energy and renewable energy. *Renew. Energy*, 180, 390-402. (DOI: 10.1016/j.renene.2022.01.066)
2. Yang, Z., Zhang, J., Kintner-Meyer, M. C., Lu, X., Choi, D., Lemmon, J. P., & Liu, J. (2011). Electrochemical energy storage for green grid. *Chem. Rev.*, 111, 3577-3613. (DOI: 10.1021/cr100290v)
3. Mahmoud, M., Ramadan, M., Olabi, A. G., Pullen, K., & Naher, S. (2020). A review of mechanical energy storage systems combined with wind and solar applications. *Energy Convers. Manag.* 210, 112670. (DOI: 10.1016/j.enconman.2020.112670)
4. Hameer, S., & van Niekerk, J. L. (2015). A review of large-scale electrical energy storage. *Int. J. Energy Res.*, 39, 1179-1195. (DOI: 10.1002/er.3294)
5. Sarbu, I., & Sebarchievici, C. (2018). A comprehensive review of thermal energy storage. *Sustainability*, 10, 191. (DOI: 10.3390/su10010191)
6. Ho, J., Jow, T. R., & Boggs, S. (2010). Historical introduction to capacitor technology. *IEEE Electr. Insul. Mag.*, 26, 20-25. (DOI: 10.1109/MEI.2010.5383924)
7. Breiter, M., Kleinerman, M., & Delahay, P. (1958). Structure of the double layer and electrode Processes1. *J. Am. Chem. Soc.*, 80, 5111-5117. (DOI:10.1021/ja01552a029)
8. Ahankari, S. S., Lasrado, D., & Ramesh, S. (2022). Advances in Materials and Fabrication of Separators in Supercapacitors. *Mater. Adv.* (DOI:10.1039/D1MA00599E)
9. Wang, G., Zhang, L., & Zhang, J. (2012). A review of electrode materials for electrochemical supercapacitors. *Chem. Soc. Rev.*, 41, 797-828. (DOI:10.1039/C1CS15060J)
10. Sung, J., & Shin, C. (2020). Recent studies on supercapacitors with next-generation structures. *Micromachines*, 11, 1125. (DOI:10.3390/mi11121125)
11. Lu, X., Wang, C., Favier, F., & Pinna, N. (2017). Electrospun nanomaterials for supercapacitor electrodes: designed architectures and electrochemical performance. *Adv. Energy Mater.*, 7, 1601301. (DOI:10.1002/aenm.201601301)

12. Chen, G. Z. (2020). Supercapattery: Merit merge of capacitive and Nernstian charge storage mechanisms. *Curr. Opin. Electrochem.*, *21*, 358-367. (DOI:10.1016/j.coelec.2020.04.002)
13. Miao, L., Song, Z., Zhu, D., Li, L., Gan, L., & Liu, M. (2020). Recent advances in carbon-based supercapacitors. *Mater. Adv.*, *1*, 945-966. (DOI:10.1039/D0MA00384K)
14. Quispe-Garrido, V., Cerron-Calle, G. A., Bazan-Aguilar, A., Ruiz-Montoya, J. G., López, E. O., & Baena-Moncada, A. M. (2021). Advances in the design and application of transition metal oxide-based supercapacitors. *Open Chem.*, *19*, 709-725. (DOI:10.1515/chem-2021-0059)
15. Chiu, K. L., & Lin, L. Y. (2019). Applied potential-dependent performance of the nickel cobalt oxysulfide nanotube/nickel molybdenum oxide nanosheet core-shell structure in energy storage and oxygen evolution. *J. Mater. Chem. A*, *7*, 4626-4639. (DOI:10.1039/c8ta11471d)
16. Liu, M., Fu, Y., Ma, H., Wang, T., Guan, C., & Hu, K. (2016). Flower-like manganese-cobalt oxysulfide supported on Ni foam as a novel faradaic electrode with commendable performance. *Electrochim. Acta*, *191*, 916-922. (DOI:10.1016/j.electacta.2016.01.156)
17. Kuai, Y., Liu, M., Wang, T., Fu, Y., Ma, H., Jiang, Q., ... & Hu, K. (2017). Sea anemone-like zinc-cobalt oxysulfides grown on Ni foam as a battery-type electrode with admirable performance. *Ionics*, *23*, 1391-1398. (DOI:10.1007/s11581-017-1981-5)
18. Asen, P., Shahrokhian, S., & Zad, A. I. (2018). Iron-vanadium oxysulfide nanostructures as novel electrode materials for supercapacitor applications. *J. Electroanal. Chem.*, *818*, 157-167. (DOI:10.1016/j.jelechem.2018.04.035)
19. Asen, P., Shahrokhian, S., & Zad, A. I. (2018). Iron-vanadium oxysulfide nanostructures as novel electrode materials for supercapacitor applications. *J. Electroanal. Chem.*, *818*, 157-167. (DOI:10.1002/er.6218)
20. Venkateshalu, S., Kumar, P. G., Kollu, P., Jeong, S. K., & Grace, A. N. (2018). Solvothermal synthesis and electrochemical properties of phase pure pyrite FeS₂ for supercapacitor applications. *Electrochim. Acta*, *290*, 378-389. (DOI:10.1016/j.electacta.2018.09.027)

21. Peng, S., Li, L., Tan, H., Cai, R., Shi, W., Li, C., ... & Yan, Q. (2014). MS₂ (M= Co and Ni) hollow spheres with tunable interiors for high-performance supercapacitors and photovoltaics. *Adv. Funct. Mater.*, *24*, 2155-2162. (DOI:10.1002/adfm.201303273)
22. Lu, W., Shen, J., Zhang, P., Zhong, Y., Hu, Y., & Lou, X. W. (2019). Construction of CoO/Co-Cu-S hierarchical tubular heterostructures for hybrid supercapacitors. *Angew. Chem.*, *131*, 15587-15593. (DOI:10.1002/anie.201907516)
23. Xie, S., Gou, J., Liu, B., & Liu, C. (2018). Synthesis of cobalt-doped nickel sulfide nanomaterials with rich edge sites as high-performance supercapacitor electrode materials. *Inorg. Chem. Front.*, *5*, 1218-1225. (DOI:10.1039/c8qi00172c)
24. Kim, B. C., Manikandan, R., Yu, K. H., Park, M. S., Kim, D. W., Park, S. Y., & Raj, C. J. (2019). Efficient supercapattery behavior of mesoporous hydrous and anhydrous cobalt molybdate nanostructures. *J. Alloys Compd.*, *789*, 256-265. (DOI:10.1016/j.jallcom.2019.03.033)
25. Iqbal, J., Li, L., Numan, A., Rafique, S., Jafer, R., Mohamad, S., ... & Ramesh, S. (2019). Density functional theory simulation of cobalt oxide aggregation and facile synthesis of a cobalt oxide, gold and multiwalled carbon nanotube based ternary composite for a high performance supercapattery. *New J. Chem.*, *43*, 13183-13195. (DOI:10.1039/c9nj02473e)
26. Padmanathan, N., Shao, H., McNulty, D., O'Dwyer, C., & Razeeb, K. M. (2016). Hierarchical NiO-In₂O₃ microflower (3D)/nanorod (1D) hetero-architecture as a supercapattery electrode with excellent cyclic stability. *J. Mater. Chem. A*, *4*, 4820-4830. (DOI:10.1039/c5ta10407f)
27. Shao, H., Padmanathan, N., McNulty, D., O' Dwyer, C., & Razeeb, K. M. (2016). Supercapattery based on binder-free CO₃(PO₄)₂·8H₂O multilayer nano/microflakes on nickel foam. *ACS Appl. Mater. Interfaces*, *8*, 28592-28598. (DOI: 10.1021/acsami.6b08354)
28. Surendran, S., Shanmugapriya, S., Sivanantham, A., Shanmugam, S., & Kalai Selvan, R. (2018). Electrospun carbon nanofibers encapsulated with NiCoP: a multifunctional electrode for supercapattery and oxygen reduction, oxygen evolution, and hydrogen evolution reactions. *Adv. Energy Mater.*, *8*, 1800555. (DOI: 10.1002/aenm.201800555)
29. Padmanathan, N., Shao, H., & Razeeb, K. M. (2018). Multifunctional nickel phosphate nano/microflakes 3D electrode for electrochemical energy storage, nonenzymatic glucose,

- and sweat pH sensors. *ACS Appl. Mater. Interfaces*, *10*, 8599-8610. (DOI: 10.1021/acsami.7b17187)
30. Chen, H. C., Qin, Y., Cao, H., Song, X., Huang, C., Feng, H., & Zhao, X. S. (2019). Synthesis of amorphous nickel–cobalt–manganese hydroxides for supercapacitor-battery hybrid energy storage system. *Energy Stor. Mater.*, *17*, 194-203. (DOI: 10.1016/j.ensm.2018.07.018)
31. Hu, Q., Tang, M., He, M., Jiang, N., Xu, C., Lin, D., & Zheng, Q. (2020). Core-shell MnO₂@ CoS nanosheets with oxygen vacancies for high-performance supercapattery. *J. Power Sources*, *446*, 227335. (DOI: 10.1016/j.jpowsour.2019.227335)
32. Heng, I., Low, F. W., Lai, C. W., Juan, J. C., Amin, N., & Tiong, S. K. (2019). High performance supercapattery with rGO/TiO₂ nanocomposites anode and activated carbon cathode. *J. Alloys Compd.*, *796*, 13-24. (DOI: 10.1016/j.jallcom.2019.04.347)
33. Brunauer, S., Emmett, P. H., & Teller, E. (1938). Adsorption of gases in multimolecular layers. *J. Am. Chem. Soc.*, *60*, 309-319. (DOI: 10.1021/ja01269a023)
34. Eddaoudi, M. (2005). Characterization of Porous Solids and Powders: Surface Area, Pore Size and Density By S. Lowell, JE Shields, MA Thomas, and M. Thommes. Kluwer Academic Publishers: Dordrecht, The Netherlands. 2004. (DOI: 10.1021/ja041016i)
35. Ratha, S., & Samantara, A. K. (2018). Supercapacitor: instrumentation, measurement and performance evaluation techniques. Springer. (DOI: 10.1007/978-981-13-3086-5)
36. Majumdar, D. (2021). Recent progress in copper sulfide based nanomaterials for high energy supercapacitor applications. *J. Electroanal. Chem.*, *880*, 114825. (DOI: 10.1016/j.jelechem.2020.114825)
37. Mathis, T. S., Kurra, N., Wang, X., Pinto, D., Simon, P., & Gogotsi, Y. (2019). Energy storage data reporting in perspective—guidelines for interpreting the performance of electrochemical energy storage systems. *Adv. Energy Mater.*, *9*, 1902007. (DOI: 10.1002/aenm.201902007)
38. Liu, J., Wang, J., Xu, C., Jiang, H., Li, C., Zhang, L., ... & Shen, Z. X. (2018). Advanced energy storage devices: basic principles, analytical methods, and rational materials design. *Adv. Sci.*, *5*, 1700322. (DOI: 10.1002/advs.201700322)
39. Gaberscek, M. (2021). Understanding Li-based battery materials via electrochemical impedance spectroscopy. *Nat. Commun.*, *12*, 1-4. (DOI: 10.1038/s41467-021-26894-5)

40. Mansfeld, F. (2003). Electrochemical methods of corrosion testing. *ASM handbook*, 13, 446-462. (DOI: 10.31399/asm.hb.v13a.a0003644)
41. Shombe, G. B., Khan, M. D., Zequine, C., Zhao, C., Gupta, R. K., & Revaprasadu, N. (2020). Direct solvent free synthesis of bare α -NiS, β -NiS and α - β -NiS composite as excellent electrocatalysts: Effect of self-capping on supercapacitance and overall water splitting activity. *Sci. Rep.*, 10, 1-14. (DOI: 10.1038/s41598-020-59714-9)
42. Sing, K. S., & Williams, R. T. (2004). Physisorption hysteresis loops and the characterization of nanoporous materials. *Adsorp. Sci. Technol.*, 22, 773-782. (DOI: 10.1515/pac-2014-1117)
43. Wan, H., Jiang, J., Yu, J., Xu, K., Miao, L., Zhang, L., ... & Ruan, Y. (2013). NiCo₂S₄ porous nanotubes synthesis via sacrificial templates: high-performance electrode materials of supercapacitors. *CrystEngComm*, 15(38), 7649-7651. (DOI: 10.1039/C3CE41243A)
44. Zanello, P., Nervi, C., & De Biani, F. F. (2019). Inorganic electrochemistry: theory, practice and application. *Royal Society of Chemistry*. (DOI: 10.1021/ja0336022)